Research Square

Preprints are preliminary reports that have not undergone peer review.
They should not be considered conclusive, used to inform clinical practice,
or referenced by the media as validated information.

Ni Doping in FeCrAl Introduces Competing Passivation and Dissolution Mechanisms in BWR Environments

Arya Chatterjee
aryac@illinois.edu

University of Illinois Urbana-Champaign
Soumita Mondal
University of Illinois Urbana-Champaign
Ronit Roy
University of Illinois Urbana-Champaign
Maryam Eslami
University of Illinois Urbana-Champaign
Janelle P. Wharry
University of Illinois Urbana-Champaign
Haozheng J. Qu
GE Vernova (United States)
Rajnikant Umretiya
GE Vernova (United States)

Article

Keywords: FeCrAl alloys, Boiling water reactor, Hydrogen water chemistry, Normal water chemistry, Hydration of Al-oxide, Spinel breakdown

Posted Date: November 11th, 2026

DOI: https://doi.org/10.21203/rs.3.rs-10941860/v1

License: This work is licensed under a Creative Commons Attribution 4.0 International License.
Read Full License

Additional Declarations: No competing interests reported.

Ni Doping in FeCrAl Introduces Competing Passivation and Dissolution Mechanisms in BWR Environments

Arya Chatterjee[a,*], Soumita Mondal[a], Ronit Roy[a], Maryam Eslami[a], Janelle P. Wharry[a,*], Haozheng J. Qu[b], Rajnikant Umretiya[b,*]

[a] The Grainger College of Engineering, Department of Mechanical Science and Engineering, University of Illinois at Urbana-Champaign, Urbana, IL, USA

[b] GE Vernova Advanced Research Center, 1 Research Circle, Schenectady, NY, USA

***Corresponding authors**.

E-mail addresses: aryac@illinois.edu (A.Chatterjee), jpw@illinois.edu (J.P. Wharry), rajnikant.umretiya@ge.com (R. Umretiya).

Abstract

The objective of this study is to understand how noble Ni additions affect FeCrAl corrosion in both oxidizing and reducing environments. FeCrAl alloys are promising accident-tolerant fuel candidates to replace Zr-based cladding, which exhibits poor high-temperature oxidation resistance. But in the Boiling Water Reactor (BWR) Hydrogen Water Chemistry (HWC) used across much of the commercial BWR fleet, FeCrAl cladding must withstand normal operation in a reducing environment, as well as survive accident scenarios in oxidizing environments. This study evaluates Fe-17.5Cr-5.5Al alloys doped with 0, 1, and 3 wt.% Ni under BWR HWC as well as Normal Water Chemistry (NWC) for six months at 288 °C. Higher-nobility Ni enables passivation and improves oxidation resistance in NWC, but can adversely affect corrosion rates in HWC. Specifically, analytical transmission electron microscopy suggests a hydrogen-assisted oxidative dissolution mechanism is driven by Al_2O_3 hydration into boehmite (AlOOH), facilitating H_2 entrapment and localized oxide failure. Because the kinetics of Ni diffusion and oxidation are sluggish, low Ni alloying concentrations (1 wt.%) exacerbate mass loss whereas higher Ni alloying concentrations (3 wt.%) allow for sufficient passivation before excessive dissolution can cause severe mass loss. Although minor Ni alloying additions can improve high-temperature oxidation resistance of FeCrAl, they may be detrimental in reducing environments. The impact of these findings reveals that designing Ni alloying additions in FeCrAl must consider competing mechanisms for accident conditions (i.e., high-temperature oxidation resistance) compared to normal operation (i.e., hydrothermal corrosion resistance) in BWRs.

Keywords: FeCrAl alloys, Boiling water reactor, Hydrogen water chemistry, Normal water chemistry, Hydration of Al-oxide, Spinel breakdown.

1. Introduction

The development of accident-tolerant fuel (ATF) cladding has gained importance following the Fukushima Daiichi Nuclear Power Plant accident. Although zirconium (Zr)-based alloys have served as the industry standard Light Water Reactor (LWR) nuclear fuel cladding for decades, their rapid exothermic oxidation and associated hydrogen generation during loss-of-coolant accidents (LOCA) present significant safety risks [1,2]. Among the leading ATF candidates, FeCrAl alloys have demonstrated exceptional high-temperature oxidation resistance (~1000-1200 °C) due to the formation of a dense, adherent α-Al_2O_3 passivating oxide layer [2–4] during simulated accident conditions [3–7]. In addition, during normal LWR operating conditions, FeCrAl alloys exhibit good hydrothermal corrosion resistance due to the formation of a protective native Cr-rich and/or Al-rich oxide layers [8,9].

The overall alloy design principle for high temperature oxidation-resistant FeCrAl alloys is to leverage the thermodynamic favorability of Al-rich oxides, together with the kinetics of Cr as an oxygen getter, in what is known as the "third element effect". Rapid Cr oxidation creates a Cr_2O_3 scale that reduces O_2 partial pressure at the metal surface, thus allowing sufficient time for Al diffusion and oxidation [10]. This generally results in a multi-layered surface oxide, with the most thermodynamically favorable (i.e., most stable) Al-oxides forming nearest the metal substrate, and the less thermodynamically favorable oxides forming as sequential outer oxide layers (i.e., Cr-oxides then outermost Fe-oxide). This "third element effect" has been demonstrated across numerous oxidation conditions and alloy compositions. For example, Chikhalikar et al. [7] demonstrated that adding 5.5 wt.% Al to Fe-21Cr alloys improved oxidation resistance at both 400 °C and 1200 °C. Similarly, Roy et al. [11] observed that Al additions in Fe-17Cr alloys positively impacted oxidation resistance at 400 °C.

The role of minor alloying elements in FeCrAl oxidation resistance is also complicated by the need to consider both kinetics and thermodynamics. One such study by Mondal, et al. investigated the synergistic effects of Cr and Mo in FeCrAl alloys [12]. They identified a "fourth element effect", in which higher Cr content promoted the formation of passivating Cr_2O_3 and Al_2O_3 layers, while Mo segregated to grain boundaries to hinder the outward diffusion of Fe and Cr [12]. Minor reactive elements have also been explored, although the thermo-kinetic competition mechanisms have not yet been fully understood. For instance, Cueff et al. [13] found that Y-coated Kanthal A1 exhibited slightly higher oxidation rates than uncoated samples due to lateral oxide growth and associated compressive stresses. Other studies have examined the role of Co in oxide dispersion strengthened (ODS) FeCrAl [14].

Thermo-kinetic competition during oxidation has emerged as an especially crucial factor for Ni alloying additions in FeCrAl, which are desirable for high-temperature mechanical strength and creep resistance. Notably, only a narrow range of Ni concentrations, up to ~3 wt.%, can be added to FeCrAl, as high Ni concentrations can destabilize the ferrite phase. But even within this relatively narrow range, numerous inconsistencies have been reported. Ni acts as an initial oxygen getter due to its higher oxygen solubility relative to Fe, subsequently serving as an oxygen source for the primary scale-formers, Cr and Al [10], thereby accelerating the passivation process. Ni also alters the chemical activity and diffusion coefficients of Al and Cr in the bulk metal matrix [15,16], leading to metallic Ni accumulation at the metal-oxide interface. This Ni stabilizes the oxide, and can also help heal or re-form oxide layers following the rupture of protective Cr/Al scales [3]. Several reports have concluded that additions of as low as only 1 wt.% Ni are sufficient to effectively limit oxidation of FeCrAl [3,17,18].

Despite the success of compositional tailoring to improve FeCrAl oxidation resistance, there is mounting evidence that such approaches may be adverse in reducing environments. Roy et al. [19] compared hydrothermal corrosion resistance of FeCrAl in Boiling Water Reactor (BWR) normal water chemistry (NWC), an oxidizing environment, to that in hydrogen water chemistry (HWC), a reducing environment. Lower-Cr alloys suffered significant deterioration in HWC due to unstable Fe-rich oxide growth and subsequent dissolution. Similarly, when probing the role of Ni on corrosion resistance of FeCrAl, Qu et al. [17] found that just 1 wt.% Ni sufficiently suppressed corrosion in BWR-NWC, although the same composition experienced the most severe mass loss in BWR-HWC. Such divergent material behaviors in these BWR environments imply altered thermo-kinetic corrosion mechanisms, which must be understood in order to design FeCrAl compositions for a range of service environments.

In the present work, we evaluate long-term hydrothermal corrosion of Fe-17Cr-5.5Al alloys having variable Ni additions (0, 1, and 3 wt.%) under simulated BWR-NWC and BWR-HWC. We describe the improvement in oxidation resistance facilitated by minor Ni additions under NWC, and contrast this with extreme mass loss facilitated by minor Ni additions under HWC. We then propose a chemical reaction pathway for accelerated hydrogen-assisted destabilization of the oxide scale in Ni-bearing alloys under HWC. This work will show that a reducing environment – particularly in long-term service – introduces additional chemical reaction pathways in Ni-doped FeCrAl which create conflicting compositional design needs for accident conditions (i.e., high-temperature oxidation resistance) compared to normal operation (i.e., hydrothermal corrosion resistance) in reducing environments like BWR-HWC.

2. Experimental

2.1. Materials and corrosion testing

Three FeCrAl alloys with varying nickel concentrations were investigated: (i) Fe-17.5Cr-5.5Al (0Ni), (ii) Fe-17.5Cr-5.5Al-1Ni, and (iii) Fe-17.5Cr-5.5Al-3Ni (all in wt.%). Rods were produced via vacuum induction melting and subsequently spin-cast from these master alloys. For each alloy, six coupons measuring approximately 11 mm × 10 mm × 2.5 mm were prepared. Each coupon included a ~1.5 mm diameter mounting hole, resulting in a net exposed surface area of approximately 350 mm^2. Prior to corrosion testing, the specimens were ground using 600-grit SiC paper and subjected to a three-step cleaning sequence: an initial wash with Liquinox, followed by isopropyl alcohol, and a final rinse in ultra-high purity (UHP) water. The initial mass of each coupon was determined by averaging three measurements taken at ambient conditions.

Three specimens per alloy were exposed to two distinct autoclave environments: BWR normal water chemistry (NWC) and BWR hydrogenated water chemistry (HWC), **Table 1**. Throughout this manuscript, samples are identified by their exposure condition and Ni content: e.g., BWR-HWC-0Ni, BWR-HWC-1Ni and BWR-HWC-3Ni and BWR-NWC-0Ni, BWR-NWC-1Ni and BWR-NWC-3Ni.

Corrosion tests were performed in recirculating autoclaves designed to simulate BWR temperature and redox potential. The test medium consisted of ultrapure water (18 MΩ·cm), without additives such as boron, lithium, or zinc. Separate autoclaves were utilized for each water chemistry, each equipped with dedicated water boards maintaining a circulation rate of ~200 cm^3/min, which provided two full volume replenishments per hour. High-purity water was preconditioned with specific gases in a 4-L glass column before being injected into the autoclave via a high-pressure pump. Pressure was maintained at ~10 MPa using a back-pressure regulator.

The effluent was continuously filtered, and water conductivity was monitored at both the inlet and outlet. Following a continuous immersion period of six months, the specimens were rinsed in UHP water then air-dried. Post-corrosion mass was determined by averaging three measurements. The area-normalized mass change (Δm_A) was calculated using the formula:

$$\Delta m_A = \frac{m_{Final} - m_{Initial}}{A} \quad (1)$$

where A is the total exposed surface area. Results are reported in mg/dm², where positive values indicate mass gain and negative values indicate mass loss.

2.2. Microstructural characterization

Surface morphology was characterized using a Thermo Scientific Helios G4 UX dual-beam scanning electron microscope (SEM) operated at 10 kV and 0.8 nA. Cross-sectional transmission electron microscopy (TEM) lamellae were prepared using the focused ion beam (FIB) milling technique on an FEI Quanta 3D SEM at the Pacific Northwest National Laboratory (PNNL). These lamellae were extracted to permit high-resolution observation of the oxide layer, the substrate, and the resultant corrosion products at the interface, following the standard procedures described in Ref. [17]. Substructural and microstructural features of the oxide were analyzed using a JEOL ARM200CF microscope operating in scanning TEM (STEM) mode and equipped with an aberration (C_s) corrector. Elemental mapping and chemical analysis were performed via STEM with energy dispersive X-ray spectroscopy (STEM-EDS) using a JEOL Centurio silicon drift detector with a 0.9 sR solid collection angle.

Table 1: Autoclave test conditions used in the current investigation.

Test designation	Test conditions	Water chemistry	Gaseous content	Temperature (°C)
BWR-HWC	Simulated Boiling Water Reactor (BWR)	Hydrogenated water chemistry (HWC)	0.3 ppm H_2 (<5 ppb O_2)	288
BWR-NWC	Simulated Boiling Water Reactor (BWR)	Normal water chemistry (NWC)	1 ppm O_2	288

3. Results

3.1. Mass change and surface topography

Fig. 1 illustrates the area-normalized mass change (Δm_A) of the FeCrAl alloys following six months of exposure. While both BWR-HWC and BWR-NWC environments induce measurable changes, the effects are opposite in nature. Exposure to BWR-HWC conditions at 288 °C results in a net mass loss across all compositions, whereas BWR-NWC exposure leads to a net mass gain, **Fig. 1**. Under NWC conditions, the magnitude of mass gain increases proportionally with Ni content, suggesting that Ni facilitates the formation of stable, protective oxide layers in oxidizing environments. Conversely, in the reducing HWC environment, all alloys experience significant mass loss. The 1Ni alloy exhibits the most pronounced weight loss, followed by the 0Ni alloy, while the 3Ni alloy shows the greatest resistance to weight loss, **Fig. 1**. These results suggest that a critical Ni threshold (e.g., 3 wt.%) is required to enhance the corrosion performance of Fe-17.5Cr-5.5Al alloys under hydrogenated conditions.

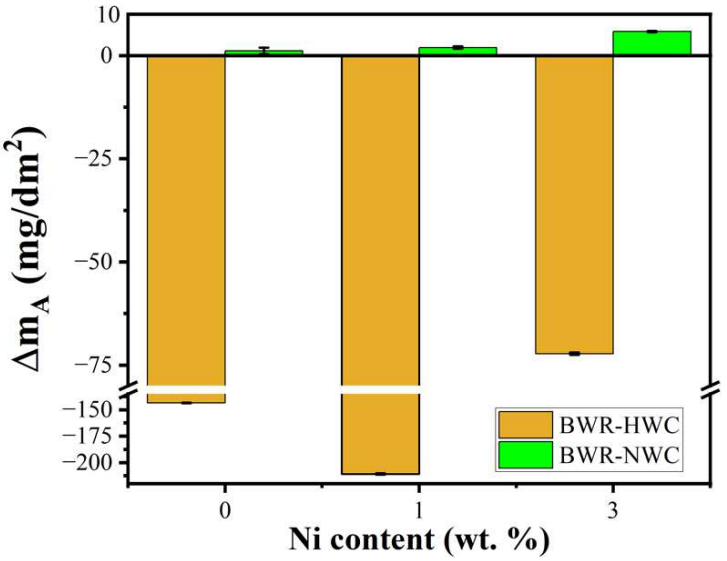


Figure 1: Weight change of all three FeCrAl alloys with different Ni contents after exposure to simulated BWR-HWC and BWR-NWC for 6 months.

The surface evolution after six months is characterized using secondary electron (SE) imaging. **Figure 2** presents top-down SEM micrographs highlighting the development and morphology of faceted spinel oxides on the exposed surface. In the NWC environment, the 0Ni alloy primarily exhibits flaky oxides (yellow arrows) after six months, **Fig. 2a**. The NWC-1Ni alloy (**Fig. 2b**) displays a combination of numerous small (<0.5 μm) polyhedral faceted nodules and occasional larger (1–2 μm) nodules, similar to the morphologies observed in the HWC samples. Finally, the NWC-3Ni alloy (**Fig. 2c**) shows a mixed morphology of roughly equal proportions of polyhedral spinel nodules and flaky oxides. While 3-month studies have previously identified these surfaces as Fe-Al-rich oxides and hematite (α-Fe_2O_3) [17], detailed characterization of the current 6-month exposure oxides will be addressed in the following sections. By contrast, in the HWC-0Ni and HWC-1Ni specimens (**Figs. 2d–e**), sparse fine (~1 μm) polyhedral spinel nodules (red arrows) are observed. With higher Ni content, the HWC-3Ni

sample (**Fig. 2f**) features significantly larger (3–8.5 µm) spinel oxides covering nearly the entire surface.

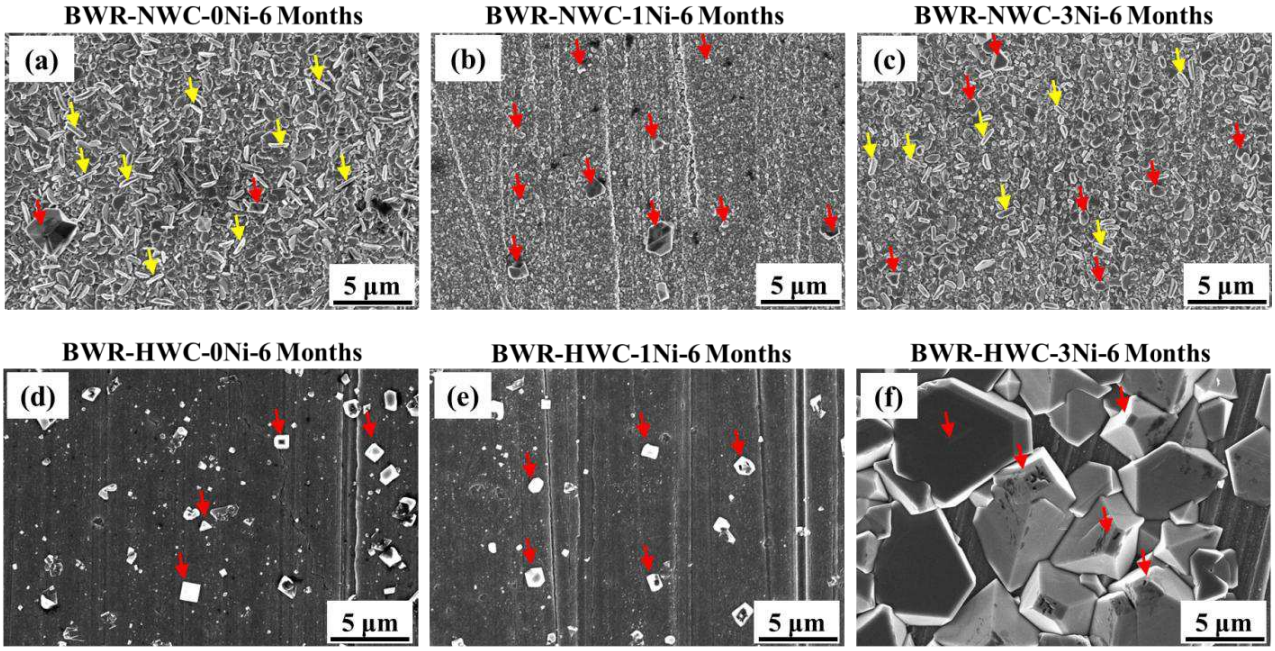


Figure 2: SEM surface morphology of FeCrAl alloys with 0, 1, and 3 wt% Ni after 6 months of exposure in simulated (a-c) BWR-NWC, and (d-f) BWR-HWC conditions. Red and yellow arrows point towards polyhedral spinel nodules and flaky oxides, respectively.

3.2. Corrosion in simulated BWR-NWC

Figure 3 presents BF-STEM cross-sectional images of the oxide layers formed after six months of exposure to BWR-NWC conditions. The average oxide thickness across all NWC specimens is approximately 0.5 µm. The oxide layer is comprised of two distinct morphologies in all three alloys (**Fig. 3a–c**): large, faceted oxide nodules at the outermost surface, and an underlying nanocrystalline inner layer adjacent to the metal substrate. While nanoscale porosity is present in all nanocrystalline layers, BWR-NWC-3Ni (**Fig. 3c**) exhibits the lowest pore number density. Notably, NWC specimens do not show any microscopic cracking or porosity at the nodule–inner layer interface. This suggests that the NWC exposure leads to formation of a continuous and

protective oxide, consistent with mass gain in all alloys, which is critical for preventing mechanical failure during long-term corrosion.

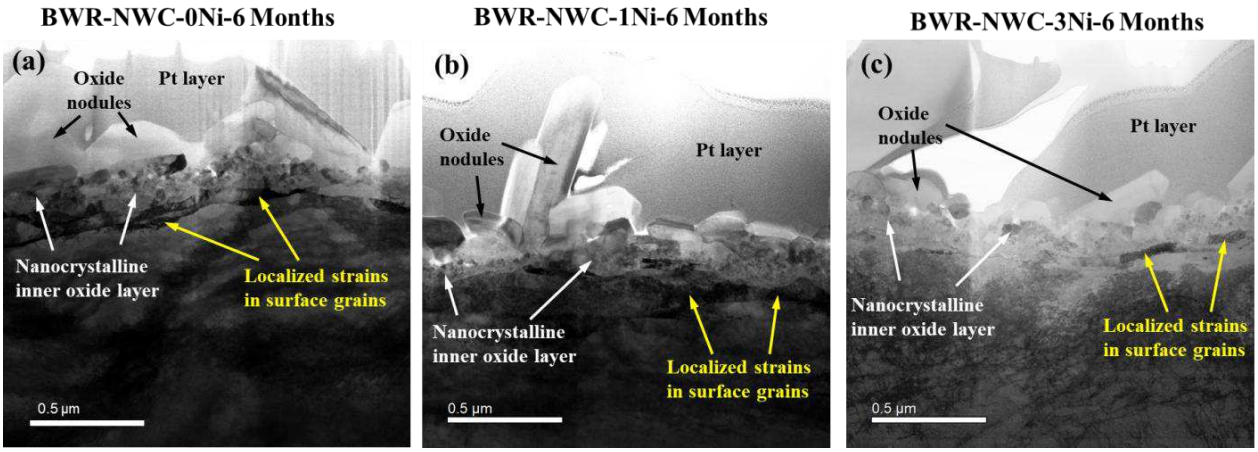


Figure 3: BF-STEM images showing cross-sectional overviews of the oxide layers for FeCrAl alloys with variable Ni contents after simulated NWC exposure for 6 months.

STEM-EDS and high-resolution (HR) HAADF-STEM analyses are used to characterize the chemical and structural evolution of these scales. In the BWR-NWC-0Ni specimen, the outer nodules are Fe-dominant. Fast Fourier Transform (FFT) analysis confirms these as hematite (Fe_2O_3), **Fig. 4a**, consistent with the flaky morphology observed via SEM (**Fig. 2a**). The underlying nanocrystalline (NC) region has a relatively uniform Fe distribution with heterogeneous Cr and Al concentrations, **Fig. 4b**. This indicates a mixed alumina/chromia layer with spatially varying co-location of Cr and Al. A 10–15 nm thick Al/Cr enrichment layer is detected at the metal-oxide interface, **Fig. 4c**.

In BWR-NWC-1Ni, the nodules consist of both Fe_2O_3 and polyhedral Fe-rich oxides, likely magnetite, **Fig. 5a**. The inner nanocrystalline layer contains Fe and Cr, with Al content even lower than in the oxide layer formed in BWR-NWC-0Ni. Ni enrichment is observed at the metal-oxide interface beneath the Al/Cr-rich layer, **Fig. 5b**. For BWR-NWC-3Ni, the surface

features elongated Fe_2O_3 nodules alongside polyhedral Ni-rich Fe spinels ($NiFe_2O_4$), as confirmed by HR HAADF-STEM and FFT analysis, **Fig. 6a**. The inner nanocrystalline layer is primarily Fe- and Cr-rich, with the lowest Al concentration across all NWC specimens. Ni enrichment at the metal-oxide interface is notably more pronounced in the 3Ni alloy, **Fig. 6b**.

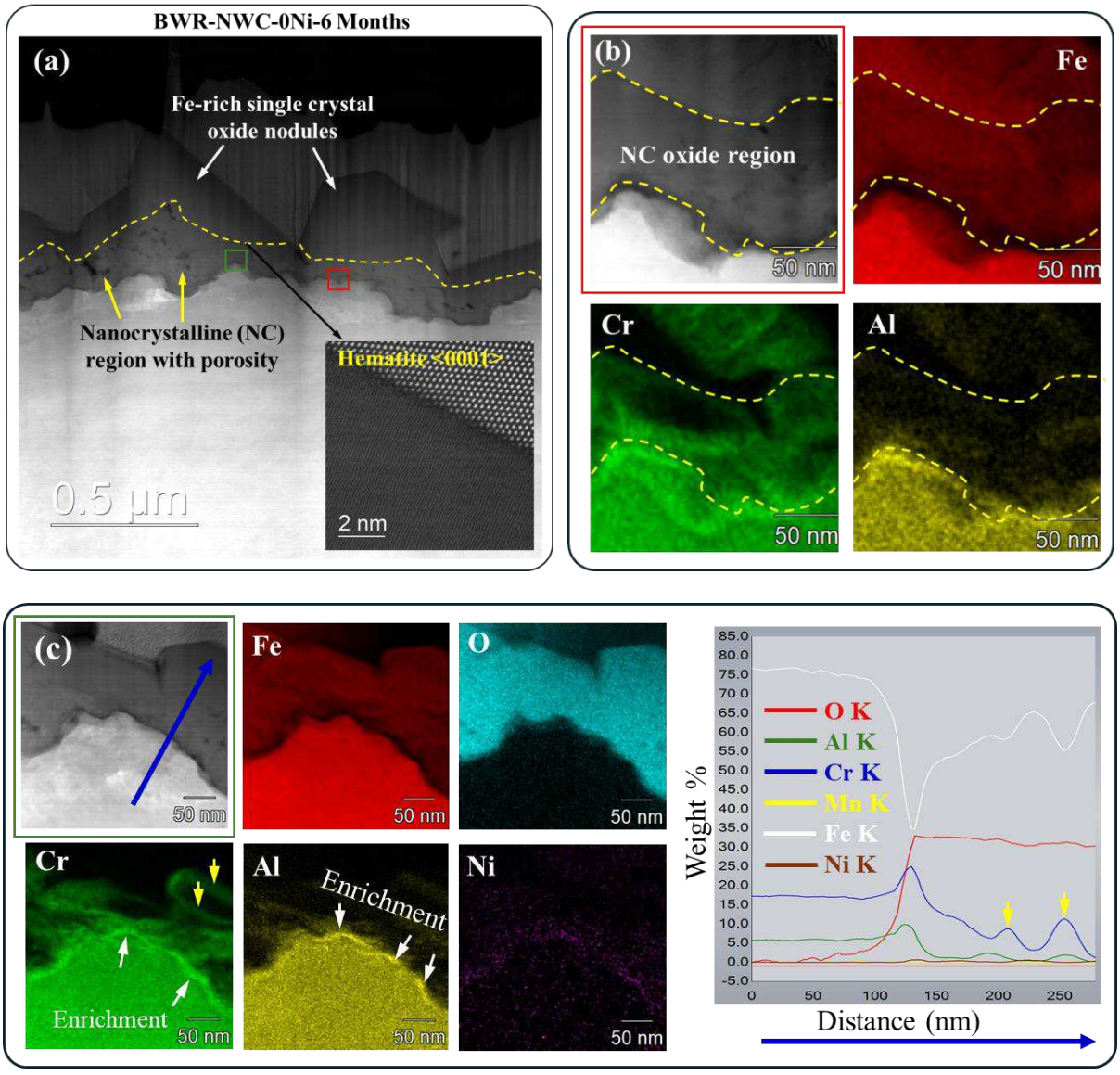


Figure 4: STEM-EDS maps showing cross-sectional overviews of the oxide layers for BWR-NWC-0Ni samples after exposure for 6 months. Enlarged views of red and green boxes in (a) are shown in (b) and (c), respectively. The blue arrow in BF-STEM image in (c) indicates EDS line profile direction.

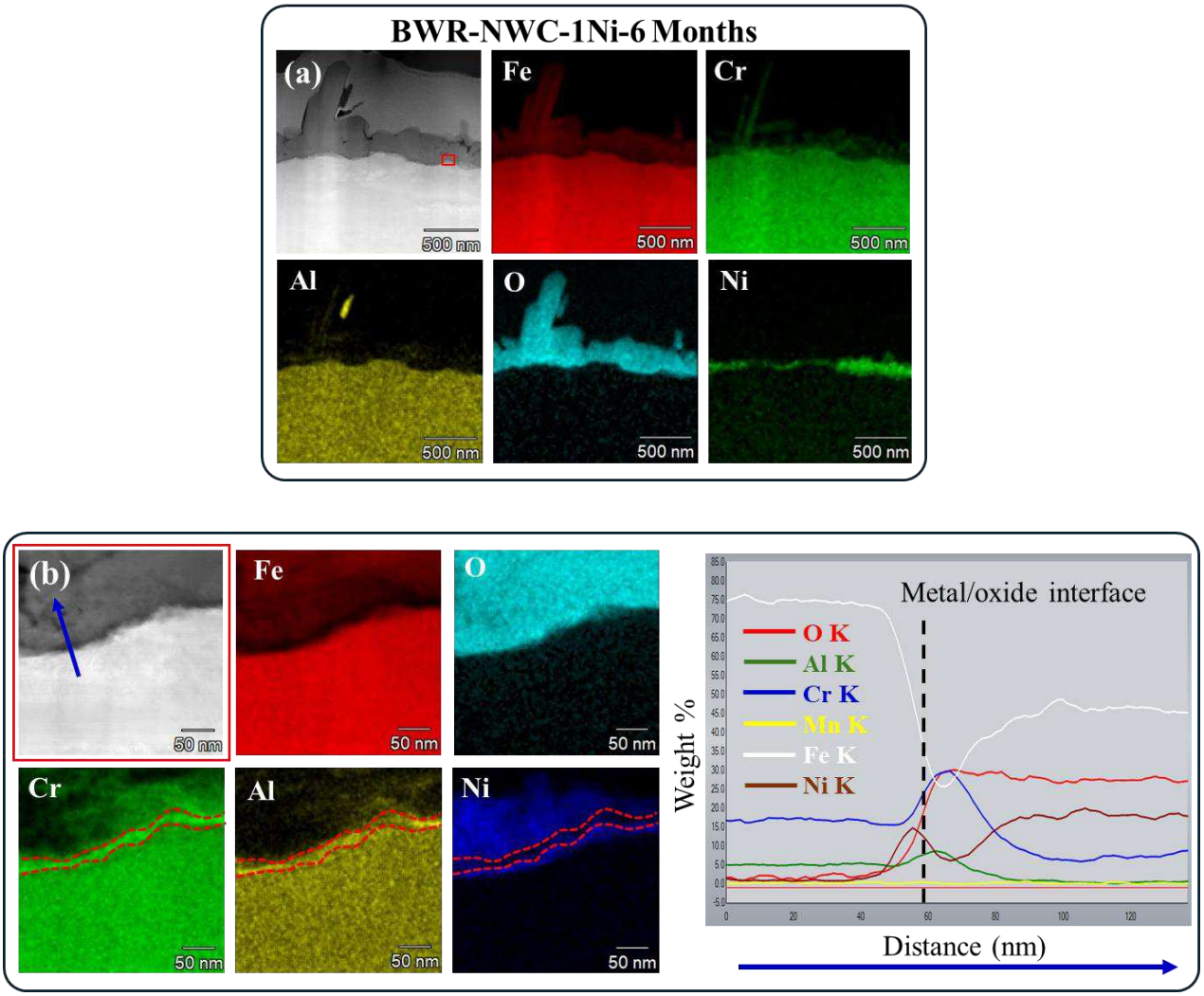


Figure 5: STEM-EDS maps showing cross-sectional overviews of the oxide layers for BWR-NWC-1Ni samples after exposure for 6 months. Enlarged view of red box in (a) is shown in (b). The blue arrow in BF-STEM image in (b) indicates EDS line profile direction.

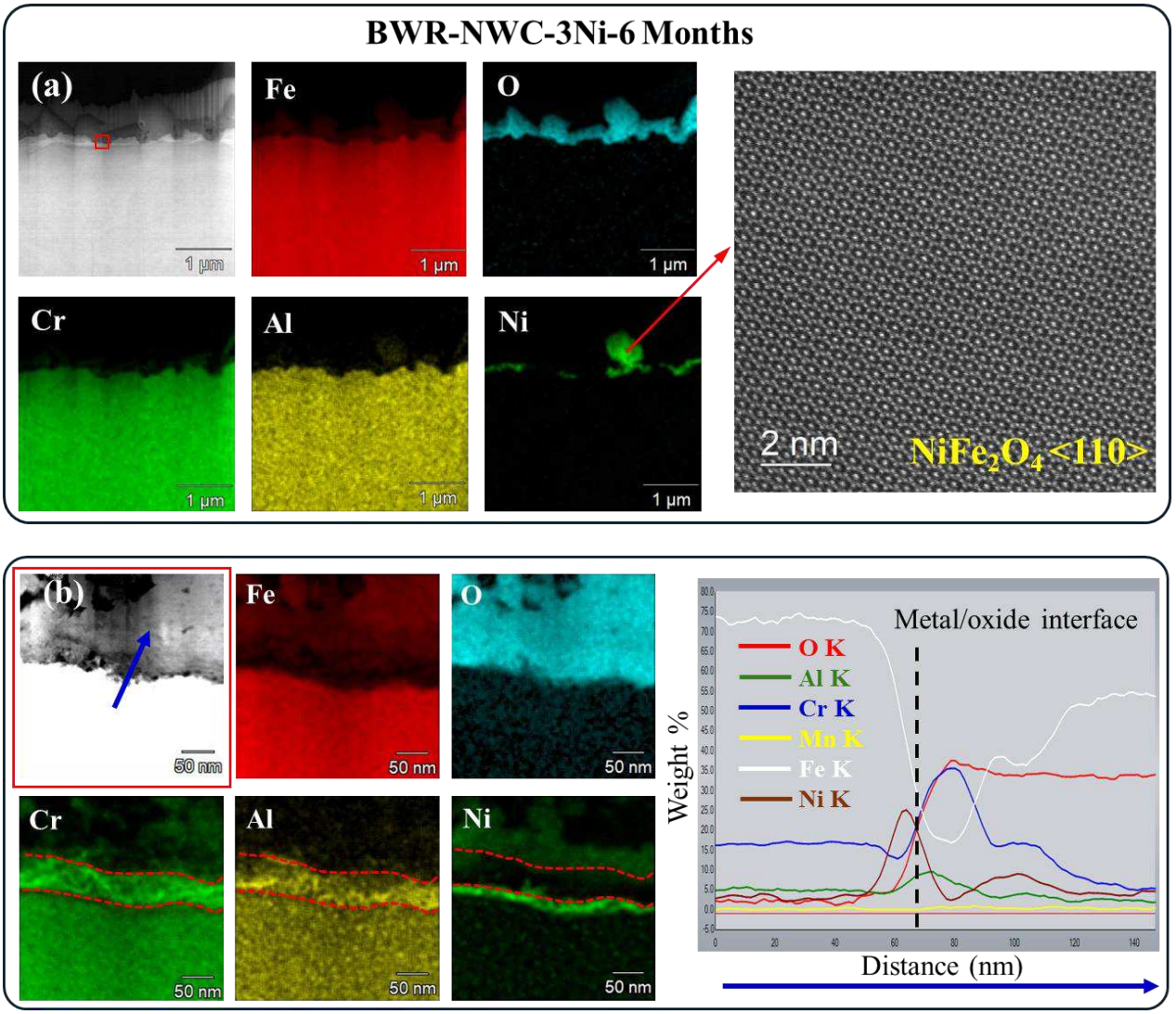


Figure 6: STEM-EDS maps showing cross-sectional overviews of the oxide layers for BWR-NWC-3Ni samples after exposure for 6 months. Enlarged view of red box in (a) is shown in (b). The blue arrow in BF-STEM image in (b) indicates EDS line profile direction.

3.3. Corrosion in simulated BWR-HWC

Figure 7 presents BF-STEM cross-sectional micrographs of the oxide layers formed on the FeCrAl alloys after six months of BWR-HWC exposure. In the 0Ni specimen, the oxide layer is largely uniform in thickness ~3 μm, with only a negligible presence of faceted polyhedral

nodules at the outermost surface, **Fig. 7a**. The 1Ni alloy exhibits similar features but with a higher frequency of both outer nodules and the inner oxide layer, **Fig. 7b**. The inner oxide is again relatively uniform in thickness ~2 µm. Notably, the interface between the outer nodules and the inner oxide in the 1Ni alloy shows a high density of cracks, which is absent in the 0Ni specimen. This cracking is attributed to the increased number of intermittent interfacial areas and the associated stress accumulation resulting from the structural mismatch between the two oxide types. Conversely, the 3Ni alloy lacks such interfacial cracking because the high volume of spinel nodules forms a nearly continuous interface with the underlying inner oxide, **Fig. 7c**.

The inner oxide exhibits greater thickness non-uniformity, generally ranging ~1-2 µm thick. Oxide layer thicknesses are as much as a factor of ~5 greater than oxide layers following BWR-NWC exposure. Together with the extensive mass loss in BWR-NWC, these results suggest extensive spallation and continuous re-oxidation in BWR-HWC environments, regardless of Ni content.

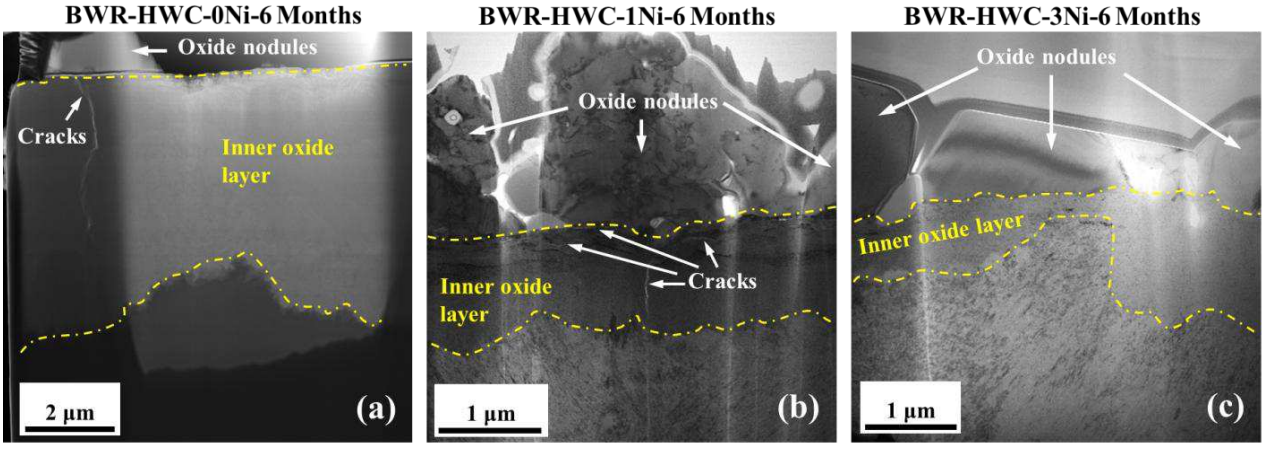
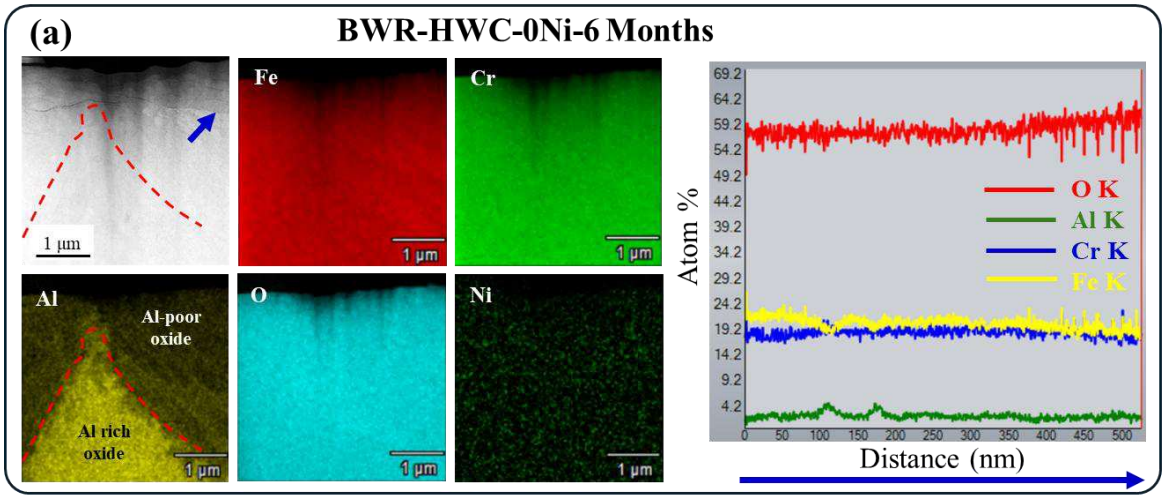


Figure 7: BF-STEM images showing cross-sectional overviews of the oxide layers for FeCrAl alloys with variable Ni contents after simulated HWC exposure for 6 months.

Elemental distributions within the oxide layers are characterized via STEM-EDS, **Fig. 8**. In the 0Ni alloy, Fe and Cr are distributed uniformly, whereas Al is inhomogeneous, showing depletion near the electrolyte and enrichment toward the metal substrate (**Fig. 8a**). This Al gradient is even more pronounced in the 1Ni alloy, with an Al concentration difference of approximately 5.2 at.% (i.e. ~5 wt.%) between the Al-rich (~8.5 at.%) and Al-poor (~3.3 at.%) regions (**Fig. 8b**). In both the 1Ni and 3Ni alloys, the Al-rich regions are significantly more porous than the Al-poor regions.

The outer spinel nodules in the 1Ni and 3Ni alloys are predominantly Fe-rich, suggesting the formation of magnetite (Fe_3O_4). This identification is consistent with the octahedral and dodecahedral oxide particles observed in SEM (**Figs. 8b** and **8c**), which are characteristic morphologies for magnetite [20,21]. While the inner oxide of the 3Ni specimen also displays Al-rich and Al-poor zones, its Al-poor region is containing less defects (porosity, cracks) than that of the 1Ni alloy. This suggests that a higher Ni content promotes the formation of a denser and more stable oxide structure within the Al-depleted zone, enhancing the overall integrity of the scale.



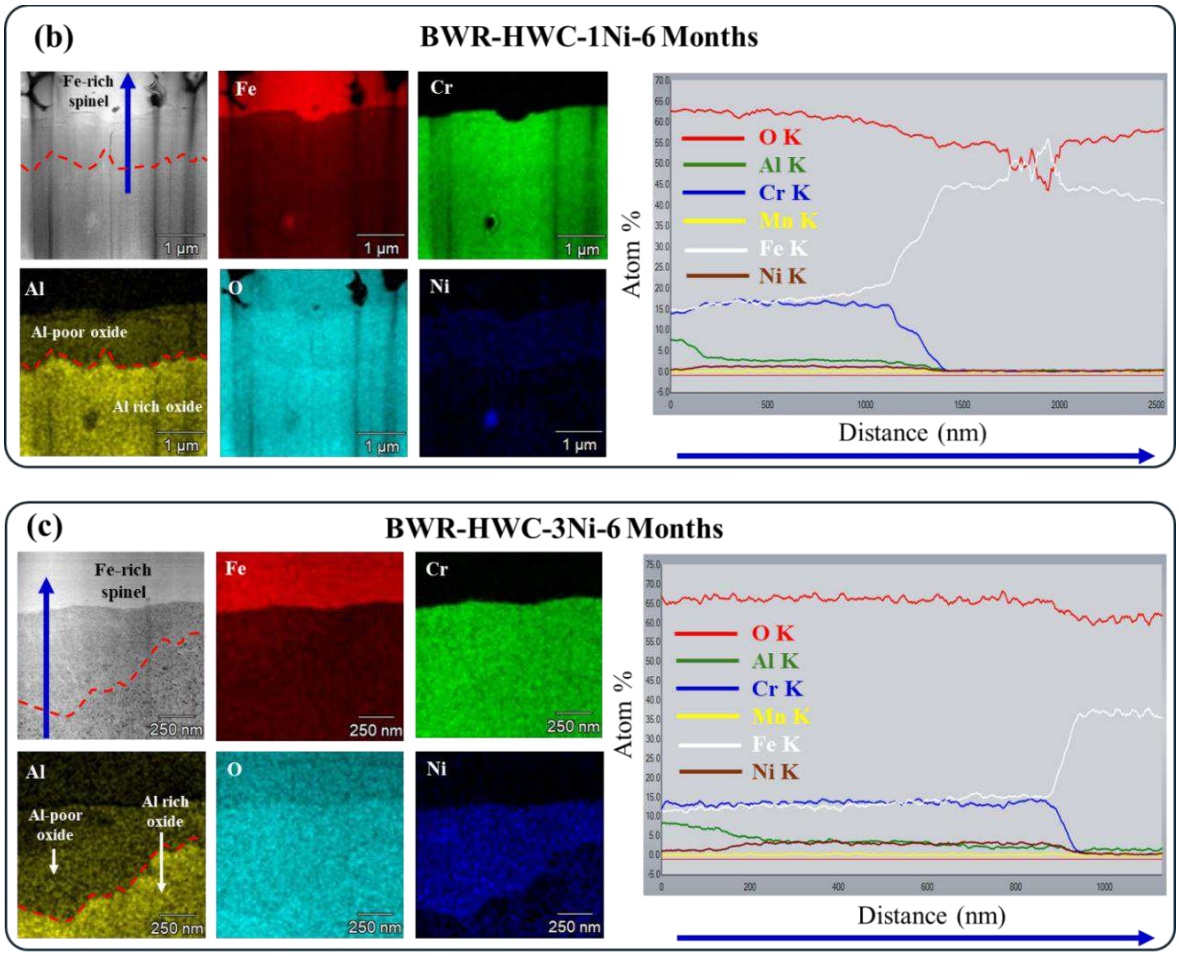


Figure 8: STEM-EDS maps and line profiles showing cross-sectional overviews of the oxide layers for FeCrAl alloys with variable Ni contents after simulated HWC exposure for 6 months. The red dashed lines in BF-STEM images indicate the interface between Al-rich and Al-poor oxide regions. The blue arrows in BF-STEM images indicate EDS line profile directions.

4. Discussion

The two water chemistries investigated affect the alloys in fundamentally different ways: BWR-HWC conditions result in net mass loss, whereas BWR-NWC conditions lead to consistent mass gain. These opposing trends are attributed to differences in the formation kinetics, chemical composition, and spatial organization of the resulting oxide layers. A comprehensive summary of

these oxide characteristics is provided in **Table 2**. The following sections discuss the specific mechanisms governing oxide evolution in each environment.

Table 2: Summary of oxide layer and alloy substrate composition evolution in BWR-HWC and BWR-NWC conditions for the duration of 6 months.

Layer	Oxide	0Ni		1Ni		3Ni	
		HWC	**NWC**	**HWC**	**NWC**	**HWC**	**NWC**
Outermost	Spinel	Fe_2O_3, $FeCrO_3$	Fe_2O_3, $FeCrO_3$	Fe_2O_3, $FeCrO_3$	Fe_2O_3, $FeCrO_3$, $NiFe_2O_4$, $NiCr_2O_4$	Fe_2O_3, $FeCrO_3$, Fe_3O_4	Fe_2O_3, $FeCrO_3$, $NiFe_2O_4$, $NiCr_2O_4$
Middle	Intermixed	Cr_2O_3, Fe-oxide	Fe-oxide	Cr_2O_3, NiO, Fe-oxide	Fe-oxide, Cr_2O_3, NiO	Cr_2O_3, NiO, Fe-oxide	Fe-oxide, Cr_2O_3, NiO
Inner	Intermixed	Al_2O_3, Cr_2O_3	N/A	Al_2O_3, Cr_2O_3	Cr_2O_3, Al_2O_3	Al_2O_3, Cr_2O_3	Cr_2O_3, Al_2O_3
Porosity in M & I layers	–	Some	Some	Most	Least	Some	Least
Segregation at alloy surface	–	N/A	N/A	N/A	Ni	N/A	Ni

4.1 Formation of Oxides in NWC

Overall, the multi-layered oxide that forms in BWR-NWC conditions follows similar formation pathways and chemical distributions that are conventionally observed during hydrothermal corrosion of FeCrAl alloys. In general, the sequential order of oxide layer compositions between the metal substrate and the corrosive environment, follows free energy or thermodynamic

stability. That is, the most stable Al-oxides comprise the inner oxides, Cr-oxides form the middle oxides, and less stable Ni- and Fe-oxides form the outer oxide layers.

In the inner oxide layer of the BWR-NWC-0Ni alloy, the protective Al-rich layer is nearly absent, while traces of Cr-rich oxide are detectable. However, as evidenced by the EDS maps in **Fig. 4(b, c)**, neither the Cr-rich nor the Fe-rich oxides are uniformly distributed, and Cr-oxide is not the predominant phase. These observations align with previous findings for these alloys after 3 months of corrosion [17], though the degradation of the Al-rich layer is significantly more pronounced after the current 6-month exposure. The EDS line profiles for all NWC alloys (**Fig. 4c, 5b** and **6b**) indicate that Fe is the primary oxide-forming element, followed by Cr. Notably, the metal-oxide interface exhibits an enrichment of Cr and Al alongside a depletion of Fe. This suggests either an outward flux of Fe toward the surface or the inward diffusion of Cr and Al away from the surface. Similar oxide formation patterns are reported by Terrani et al. in FeCrAl alloys after one year of exposure to simulated BWR-NWC conditions [22].

The absence of a discrete Al-oxide layer within the inner oxide of the NWC alloys suggests potential spallation. This can be attributed to the Pilling-Bedworth (P-B) ratio, which is the ratio of the molar volume of the oxide to the molar volume of the metal consumed. Oxides with P-B ratios between 1 and 2 are often susceptible to spallation [23,24], a process that can lead to peeling, folding, and the subsequent formation of porosity [12]; the P-B ratio of Al_2O_3 is 1.79. The nanoscale porosity observed in STEM images of the inner oxide layers (**Fig. 4**) further supports this mechanism. Meanwhile, the outward migration of Fe results in its oxidation into hematite (Fe_2O_3), characterized by its typical flaky morphology [25], which provides a degree of protection for the 0Ni alloy.

In the Ni-bearing alloys exposed to BWR-NWC, Ni appears to substitute for Al within the inner oxide layer. In the BWR-NWC-1Ni alloy, Ni addition leads to the formation of NiO, as indicated by the increased Ni concentration in the EDS profile, **Fig. 5b**. The presence of Cr_2O_3 at the Ni–NiO interface (indicated by the red dotted line in **Fig. 5b**) further stabilizes a Ni–Cr_2O_3–NiO arrangement [26], a configuration also observed in the BWR-NWC-3Ni alloy (**Fig. 6b**). Additionally, a portion of the NiO likely reacts with Fe_2O_3 to form $NiFe_2O_4$ spinel, confirmed by the presence of polyhedral spinel nodules on the outer oxide surface (**Fig. 6a**).

With higher Ni content (3 wt.%), NiO may also react with Cr_2O_3 to form $NiCr_2O_4$ spinel within the inner oxide layer. This reaction potentially explains the lower Ni concentration relative to Cr in the inner layer of the 3Ni alloy, whereas the 1Ni alloy exhibits a higher Ni/Cr ratio. Furthermore, the scale becomes more stable with increasing Ni content. This is evidenced by both the increase in Cr concentration and the thickening of the Cr-rich regions at the interface: approximately 27 nm (~35 wt.% Cr) for the 3Ni alloy, 21 nm (~28 wt.% Cr) for the 1Ni alloy, and 15 nm (~24 wt.% Cr) for the 0Ni alloy, **Fig. 4c, 5b** and **6b**. The proposed reactions for these processes are:

$$NiO + Fe_2O_3 \rightarrow NiFe_2O_4 \quad (11)$$

$$NiO + Cr_2O_3 \rightarrow NiCr_2O_4 \quad (12)$$

The oxide distributions for the samples after 6 months in BWR-NWC condition are presented schematically in **Fig. 10**.

4.2 Formation of Oxides in HWC

Nominally, BWR-HWC oxide layers follow a similar sequence as in BWR-NWC: inner Al-rich oxides, middle Cr-rich oxides, and outer Fe-rich spinels. However, the oxides are more porous and less distinct than resulting from BWR-NWC conditions, which leads to different Ni distributions in the oxide layers. Sluggish diffusion and oxidation kinetics of Ni compete with the rapid kinetics of hydrogen adsorption, which compromises the efficacy of Ni to contribute to passivation, particularly when Ni concentrations are too low.

The population of large, Fe-rich oxide nodules is significantly lower in BWR-HWC-0Ni and -1Ni compared to BWR-HWC-3Ni. These nodules primarily consist of Fe, suggesting the hematite (Fe_2O_3) or magnetite (Fe_3O_4) phases. From a thermodynamic perspective, however, the oxidation process is not expected to initiate with these Fe-rich species. According to the Ellingham diagram, Al and Cr exhibit the lowest Gibbs free energy change (ΔG) for oxidation among the major constituent elements (Al < Cr < Fe < Ni) [27]. Consequently, the initial stages of corrosion will be dominated by the formation of a protective Al_2O_3 passivation layer, followed by Cr_2O_3.

While previous studies of the same FeCrAl alloys after 3 months of exposure showed a uniform Al and Cr distribution indicative of an effective Al_2O_3 passivation layer [17], the current 6-month data reveals a transition to two distinct regions with varying Al concentrations. This shift suggests the eventual breakdown of the Al_2O_3 barrier. Although metallic Al is typically protected from direct reaction with pure water by the existing oxide scale, hydrothermal hydration can occur when the environment is modified by the presence of α- Al_2O_3 and γ-Al_2O_3 [28,29].

Deng et al. [30,31] proposed a hydration mechanism for Al_2O_3 where, during an initial induction stage, hydrolysis breaks Al–O–Al bonds to form Al–OH species. Once the initial Al_2O_3 film is fully hydrated, OH^- ions (or H_2O molecules) become the most mobile species

within the scale, surpassing H^+, O^{2-}, or Al^{3+}. Driven by an internal anodic potential toward the alloy-oxide interface [32], these OH^- ions react with Al to form an oxy-hydroxide phase (AlOOH, Equation 2), which subsequently interacts with the remaining Al_2O_3 to generate H_2 gas (Equation 3):

$$Al_2O_3 + H_2O \rightarrow 2AlOOH \quad (2)$$

$$6AlOOH + 2Al \rightarrow 3Al_2O_3 + 4H_2 \quad (3)$$

The formation of boehmite (γ-AlOOH) during hydrothermal corrosion of Al is well-documented at temperatures between 250-350 °C [33–35], supporting the occurrence of this hydration phenomenon in the current study conducted at 288 °C. Moreover, the formed H_2 gas is expected to be entrapped as gas bubbles owing to their significantly lower permeability (factor of 100-2000) through Al_2O_3 than metallic Al [36,37]. This mechanism of H_2 evolution and entrapment is further corroborated by the porosity observed within the inner oxide layers of the BWR-HWC alloys (**Fig. 9**).

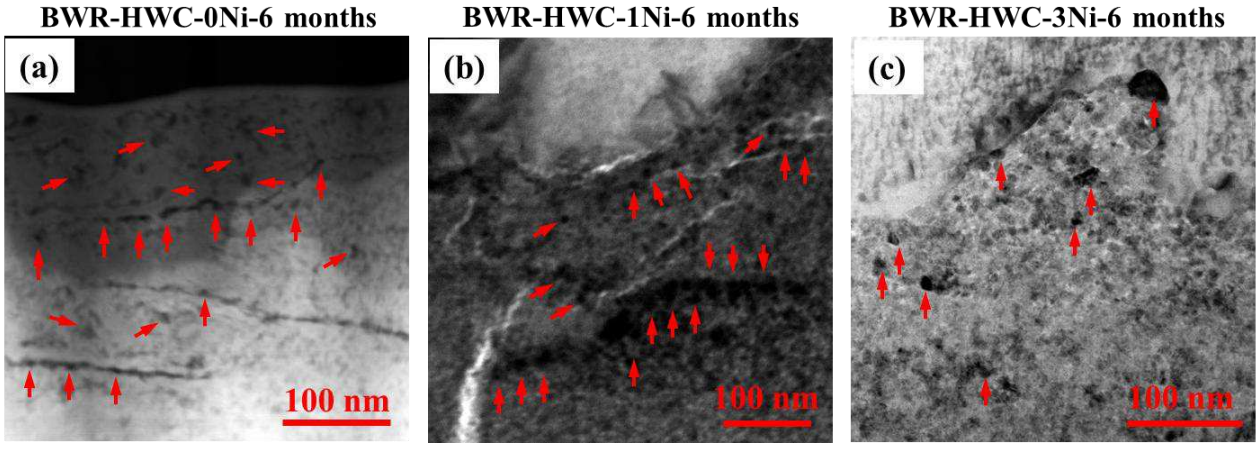


Figure 9: STEM images showing pores (indicated by red arrows) in the oxide layers for FeCrAl alloys with variable Ni contents after simulated BWR-HWC exposure for 6 months.

Since the Cr concentration remains uniform across both the Al-rich and Al-poor oxide regions, Cr_2O_3 is present throughout the entire oxide scale. Consequently, the entrapped hydrogen is expected to interact with Cr_2O_3 either through reduction [38,39] or either adsorption or chemisorption [40–43]. Reduction of Cr_2O_3 can be expressed as:

$$Cr_2O_3 + 3H_2 \rightarrow 2Cr + 3H_2O \quad (4)$$

This reaction has equilibrium constant and free energy [44] of:

$$K_C = [H_2O]^3 \bullet [Cr]^2 / [H_2]^3 \bullet [Cr_2O_3]^2 \quad (5)$$

$$\Delta G^0 = 373{,}422 - 89.22T\ J \bullet mol^{-1} \quad (6)$$

The equilibrium concentration ratio of $[H_2O] / [H_2]$ is 2.8×10^{-4} at 1000°C and 3.2×10^{-5} at 800°C [45]. Based on equations (5) and (6), this reduction reaction is only feasible in an oxygen-free, dry hydrogen environment where water vapor is continuously removed from the reaction zone. As these conditions are not present in the current hydrothermal investigation, it is more likely that the interaction occurs via adsorption or chemisorption.

In the adsorption model, hydrogen molecules or atoms form strong bonds with oxygen atoms, adhering to the surface at Cr=O and O sites [41]. In this context, the nanoporosity observed in the Al-rich region (which is intermixed with Cr-based oxides) likely provides additional surface area for hydrogen adsorption onto Cr_2O_3 crystals. Chemisorption, by contrast, requires hydrogen to be absorbed into the Cr_2O_3 lattice. Previous studies on standalone Cr_2O_3 have noted H_2 absorption and the formation of Cr(II) species between room temperature and 600 °C [40,42]; adsorption and chemisorption processes have rapid kinetics.

Regardless of the specific absorption mechanism, it is reasonable to conclude that the Cr_2O_3 layer interacts with hydrogen, leading to surface degradation through the generation of

ionic defects within the passivating film [46]. Furthermore, the $FeCr_2O_4$ spinel oxide, which typically forms within the first 3 months [17], is also susceptible to the hydrogenated environment. Mott–Schottky analysis of Fe-Cr-Ni alloys indicates that hydrogen can induce the reduction of $FeCr_2O_4$ to metallic Cr and Fe [46]. Although this does not result in the total decomposition of the protective oxide, the surface loses its passivity over time. This weakened barrier facilitates further hydrogen absorption and subsequent hydrogen embrittlement [46]. The large cracks observed within the inner oxide layers of the BWR-HWC specimens (**Fig. 7**) are likely a physical manifestation of this embrittlement.

In BWR-HWC-*x*Ni alloys, the presence and permeation of hydrogen significantly influences the oxide structure due to the high affinity of hydrogen for Fe-Ni and FeCrAl alloys [47–49]. During hydrothermal corrosion, Ni typically forms NiO [50,51], which is subsequently reduced to metallic Ni by dissolved or permeated hydrogen. This metallic Ni then reacts with hydrogen ions (H^+), leading to oxidative dissolution into Ni ions that are released into the water [52,53]. The outward transport of metal atoms is governed by the inward migration of cation vacancies through the oxide layer [54–56]. During diffusion within the oxide, H atoms ionize and donate an electron. This electron couples with an electron hole, increasing the cation vacancy density according to the following reaction:

$$½O_2 = O_{NiO} + 2h^* + V_M^{n-}, \quad (7)$$

where O_{NiO} represents an oxygen atom at an oxygen site within the NiO lattice, h* is an electron hole, V_M^{n-} is a metal cation vacancy. This mechanism facilitates the accelerated outward transportation of metal atoms [57].

Furthermore, the Fe-Ni spinel ($NiFe_2O_4$) identified in the BWR-HWC-1Ni alloy after 3 months of exposure [17] is also susceptible to reduction by permeated hydrogen. The dissociation

of this spinel releases Ni, which then undergoes oxidative dissolution [53]. The near-absence of polyhedral oxide nodules – characteristic of Fe-Ni spinels – in the 1Ni specimen after 6 months supports this reduction model. The relevant reactions are:

$$NiO + H_2 \rightarrow Ni + H_2O \quad (8)$$

$$3NiFe_2O_4 + 4H_2 \rightarrow 3Ni + 2Fe_3O_4 + 4H_2O \quad (9)$$

$$Ni + 2H^+ \rightarrow Ni^{2+} + H_2 \text{ (oxidative dissolution of Ni and release in water)} \quad (10)$$

As a result, the protection provided by the passive spinel oxide in the BWR-HWC-1Ni alloy diminishes over time, leading to the significant weight loss observed after 6 months, **Fig. 1**. In contrast, BWR-HWC-3Ni exhibits superior stability than the lower-Ni specimens. The higher Ni concentration provides a critical Ni reservoir that counteracts the slow diffusion and oxidation kinetics of Ni, enabling the alloy to withstand the reduction and subsequent oxidative dissolution processes. The remaining Ni is sufficient to maintain stable Fe-Ni spinel nodules, which continue to provide effective protection and result in the lower mass loss observed in the 3Ni specimens after 6 months (**Fig. 1**). The spatial distributions of oxides after 6 months of hydrothermal corrosion in BWR-HWC are schematically depicted in **Fig. 10.**

Ni-doped FeCrAl alloys therefore exhibit distinct material behaviors in reducing BWR-HWC than in oxidizing BWR-NWC environments. The Ni content makes these alloys extremely susceptible to hydrogen-assisted oxide dissolution, forming porosity. This leads to excessive spallation and cracking of the oxide, if insufficient Ni is present to overcome competing chemical reaction rates. Thus, while Ni doping is an effective strategy to improve FeCrAl high-temperature oxidation resistance, such a strategy is detrimental in reducing environments. Thus,

alloy design and tailoring of FeCrAl compositions to provide necessary performance in accident conditions may be incompatible in normal BWR-NWC service.

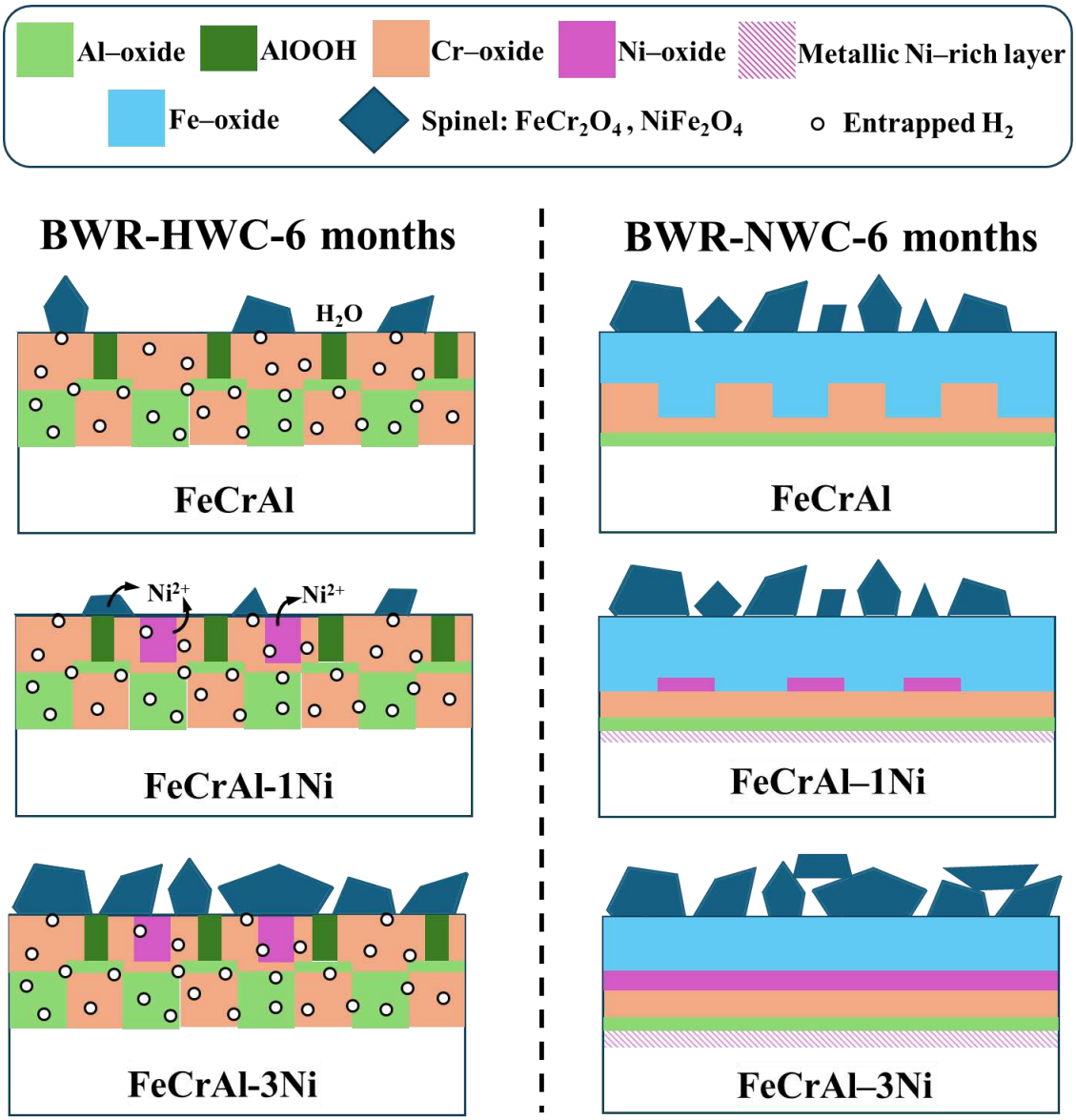


Figure 10: Schematic illustration of the oxide distributions for FeCrAl alloys exposed to simulated BWR- HWC and BWR-NWC conditions for 6 months.

5. Conclusions

The hydrothermal corrosion behavior of Ni-doped Fe-17Cr-5.5Al alloys (0, 1, and 3 wt.% Ni) was evaluated under simulated BWR-HWC and BWR-NWC conditions for six months. While Ni doping enhances resistance to oxidizing BWR-NWC environments, it can have adverse effects and actually accelerate corrosion in reducing BWR-HWC environments. We propose a rapid chemical reaction pathway in HWC that leads to hydrogen-assisted dissolution of Ni-bearing oxide scale. Since Ni oxidation is kinetically slower, low Ni concentrations are insufficient to promote passivation before excessive dissolution can destabilize the oxide to cause excessive spalling. Higher Ni concentrations are needed to overcome its sluggish passivation kinetics and limit mass loss during long-term service. Thus, while Ni doping is an effective strategy to improve FeCrAl high-temperature oxidation resistance, such a strategy is detrimental in reducing environments. These findings imply accident conditions (i.e., high-temperature oxidation resistance) and to normal operation (i.e., hydrothermal corrosion resistance) in reducing environments like BWR-HWC demand conflicting needs for FeCrAl compositional design, especially involving Ni alloying additions.

Acknowledgements

The authors declare that the research was conducted in the absence of any commercial or financial relationships that could be construed as a potential conflict of interest. Funding support from Global Nuclear Fuel (GNF), GE Vernova Advanced Research (GEVAR), and GE Hitachi Nuclear is gratefully acknowledged. Materials were synthesized with support from the U.S. Department of Energy, Office of Nuclear Energy, contract DE-NE0009047. Work at the University of Illinois was supported by the U.S. Department of Energy, Office of Nuclear

Energy, contracts DE-NE0009389 and DE-NE0009513. This report was prepared as an account of work sponsored by an agency of the United States Government. Neither the United States Government nor any agency thereof, nor any of their employees, makes any warranty, express or implied, or assumes any legal liability or responsibility for the accuracy, completeness, or usefulness of any information, apparatus, product, or process disclosed, or represents that its use would not infringe privately owned rights. Reference herein to any specific commercial product, process, or service by trade name, trademark, manufacturer, or otherwise does not necessarily constitute or imply its endorsement, recommendation, or favoring by the United States Government or any agency thereof. The views and opinions of the authors expressed herein do not necessarily state or reflect those of the United States Government or any agency thereof. The funder was not involved in the study design, collection, analysis, interpretation of the data, the writing of this article, or the decision to submit it for publication.

Data availability

Data will be made available on request.

References

1. Moalem, M. & Olander, D. R. Oxidation of Zircaloy by steam. *J. Nucl. Mater.* **182**, 170–194 (1991).

2. Hofmann, P. Current knowledge on core degradation phenomena, a review. *J. Nucl. Mater.* **270**, 194–211 (1999).

3. Jiang, G. *et al.* Corrosion of FeCrAl alloys used as fuel cladding in nuclear reactors. *J.*

Alloys Compd. **869**, 159235 (2021).

4. Park, D. J. *et al.* A study of the oxidation of FeCrAl alloy in pressurized water and high-temperature steam environment. *Corros. Sci.* **94**, 459–465 (2015).

5. Rebak, R. B. *Accident-tolerant materials for light water reactor fuels*. (Elsevier, 2020).

6. Unocic, K. A., Yamamoto, Y. & Pint, B. A. Effect of Al and Cr content on air and steam oxidation of FeCrAl alloys and commercial APMT alloy. *Oxid. Met.* **87**, 431–441 (2017).

7. Chikhalikar, A. *et al.* Effect of aluminum on the FeCr(Al) alloy oxidation resistance in steam environment at low temperature (400 °C) and high temperature (1200 °C). *Corros. Sci.* **209**, 110765 (2022).

8. Rebak, R. B. Iron-chrome-aluminum alloy cladding for increasing safety in nuclear power plants. *EPJ Nucl. Sci. Technol.* **3**, 34 (2017).

9. Rebak, R. B. Versatile oxide films protect FeCrAl alloys under normal operation and accident conditions in light water power reactors. *Jom* **70**, 176–185 (2018).

10. Huang, J. *et al.* High-temperature oxidation behavior and mechanism of a new type of wrought Ni–Fe–Cr–Al superalloy up to 1300° C. *Oxid. Met.* **53**, 273–287 (2000).

11. Roy, I. *et al.* Effect of Al concentration on Fe-17Cr alloy during steam oxidation at 400° C. *Corros. Sci.* **217**, 111135 (2023).

12. Mondal, S. *et al.* Synergistic roles of Cr and Mo in low temperature steam oxidation of FeCrAl alloys. *Corros. Sci.* **255**, 113107 (2025).

13. Cueff, R. *et al.* Effect of reactive element oxide coating on the high temperature oxidation behaviour of FeCrAl alloys. *Appl. Surf. Sci.* **229**, 233–241 (2004).

14. Zhang, S., Hayashi, S., Ukai, S. & Oono, N. H. Effect of Co addition on the high-temperature oxidation behavior of oxide-dispersion-strengthened FeCrAl alloys. *Corros. Sci.* **184**, 109391 (2021).

15. Raiman, S. S., Field, K. G., Rebak, R. B., Yamamoto, Y. & Terrani, K. A. Hydrothermal corrosion of 2nd generation FeCrAl alloys for accident tolerant fuel cladding. *J. Nucl. Mater.* **536**, 152221 (2020).

16. Kuang, W., Wu, X., Han, E.-H. & Ruan, L. Effect of nickel ion from autoclave material on oxidation behaviour of 304 stainless steel in oxygenated high temperature water. *Corros. Sci.* **53**, 1107–1114 (2011).

17. Qu, H. J. *et al.* Effect of nickel on the oxidation behavior of FeCrAl alloy in simulated PWR and BWR conditions. *Corros. Sci.* **216**, 111093 (2023).

18. Bermudez, S., Erdogan, F., Davis, V., Rojas, J. V & Umretiya, R. V. Effect of nickel on the FeCrAl alloy oxidation resistance in steam environment at high temperature (1000 ◦ C). *Nucl. Mater. Energy* **44**, 101972 (2025).

19. Roy, R. *et al.* Sequential oxidation and hydrothermal corrosion of FeCrAl alloys at BWR top-of-core conditions. *Corros. Sci.* **252**, 112965 (2025).

20. University of Minnesota's Mineral Pages: Magnetite. (2025).

21. Web page of Geology.com: Magnetite and Lodestone. https://geology.com/minerals/magnetite.shtml (2025).

22. Terrani, K. A. *et al.* Uniform corrosion of FeCrAl alloys in LWR coolant environments. *J. Nucl. Mater.* **479**, 36–47 (2016).

23. Nii, K. High temperature oxidation of alloys. *Corros. Eng.* **26**, 389–400 (1977).

24. Xu, C. & Gao, W. Pilling-Bedworth ratio for oxidation of alloys. *Mater. Res. Innov.* **3**, 231–235 (2000).

25. Itoh, H. & Sugimoto, T. Systematic control of size, shape, structure, and magnetic properties of uniform magnetite and maghemite particles. *J. Colloid Interface Sci.* **265**, 283–295 (2003).

26. Bates, M. K., Jia, Q., Ramaswamy, N., Allen, R. J. & Mukerjee, S. Composite Ni/NiO-Cr2O3 catalyst for alkaline hydrogen evolution reaction. *J. Phys. Chem. C* **119**, 5467–5477 (2015).

27. Stratton, P. Ellingham diagrams - their use and misuse. *Int. Heat Treat. Surf. Eng.* **7**, 70–73 (2013).

28. Wang, H. W., Chung, H. W., Teng, H. Te & Cao, G. Generation of hydrogen from aluminum and water - Effect of metal oxide nanocrystals and water quality. *Int. J. Hydrogen Energy* **36**, 15136–15144 (2011).

29. Chaklader, C. D. A. Hydrogen generation from water split reaction. *US Patent 2002* vol. 1 (2002).

30. Deng, Z. Y., Ferreira, J. M. F. & Sakka, Y. Hydrogen-Generation Materials for Portable Applications. *J. Am. Ceram. Soc.* **91**, 3825–3834 (2008).

31. Deng, Z. Y., Ferreira, J. M. F., Tanaka, Y. & Ye, J. Physicochemical mechanism for the continuous reaction of γ-Al2O3-modified aluminum powder with water. *J. Am. Ceram. Soc.* **90**, 1521–1526 (2007).

32. Bunker, B. C. *et al.* Hydration of passive oxide films on aluminum. *J. Phys. Chem. B* **106**, 4705–4713 (2002).

33. Shkolnikov, E. I., Shaitura, N. S. & Vlaskin, M. S. Structural properties of boehmite produced by hydrothermal oxidation of aluminum. *J. Supercrit. Fluids* **73**, 10–17 (2013).

34. Vlaskin, M. S., Shkolnikov, E. I. & Bersh, A. V. Oxidation kinetics of micron-sized aluminum powder in high-temperature boiling water. *Int. J. Hydrogen Energy* **36**, 6484–6495 (2011).

35. Kannan, T. S., Panda, P. K. & Jaleel, V. A. Preparation of pure boehmite, α-Al2O3 and their mixtures by hydrothermal oxidation of aluminium metal. *J. Mater. Sci. Lett.* **16**, 830–834 (1997).

36. Song, W., Du, J., Xu, Y. & Long, B. A study of hydrogen permeation in aluminum alloy treated by various oxidation processes. *J. Nucl. Mater.* **246**, 139–143 (1997).

37. Schlüter, H.-J., Züchner, H., Braun, R. & Buhl, H. Diffusion of hydrogen in aluminium. *Zeitschrift fuer Phys. Chemie* **181**, 103–109 (1993).

38. Baukloh, W. & Henke, G. Reduction of Chromium Oxide With Hydrogen and Solid Carbon. *Z. Anorg. Allg. Chem.* **234**, 5 (1937).

39. Chu, W. F. & Rahmel, A. The kinetics of the reduction of chromium oxide by hydrogen. *Metall. Trans. B* **10**, 401–407 (1979).

40. Fouad, N. E. Formation id Cr(II) species in the H2/CrO3 sytems-parameter control. *J. Therm. Anal. Calorim.* **60**, 541–547 (2000).

41. Nigussa, K. N., Nielsen, K. L., Borck, Ø. & Støvneng, J. A. Adsorption of hydrogen, chlorine, and sulfur atoms on a-Cr2O3(0001) surfaces: A density functional theory investigation. *Corros. Sci.* **53**, 3612–3622 (2011).

42. Ostrovskii, V. E., Kadyshevich, E. A., Gostev, B. V. & Lapidus, A. L. An adsorption and

calorimetric study of the interaction of hydrogen with chromium oxide. *Russ. J. Phys. Chem. A* **82**, 1626–1632 (2008).

43. Selwood, P. W. Hydrogen adsorption and parahydrogen conversion over chromia supported on α-alumina. *J. Catal.* **12**, 263–270 (1968).

44. Kubaschewski, O. & Slough, W. Recent progress in metallurgical thermochemistry. *Prog. Mater. Sci.* **14**, 3–54 (1969).

45. Chu, W. F. & Rahmel, A. The kinetics of the reduction of chromium oxide by hydrogen. *Metall. Trans. B* **10**, 401–407 (1979).

46. Örnek, C. *et al.* Understanding passive film degradation and its effect on hydrogen embrittlement of super duplex stainless steel – Synchrotron X-ray and electrochemical measurements combined with CalPhaD and ab-initio computational studies. *Appl. Surf. Sci.* **628**, (2023).

47. Pamungkas, M. A. *et al.* Comparative Molecular Dynamics Study of the Temperature-Dependent Performance of NiFe and Graphite Catalysts in Methane Decomposition for Hydrogen Production. *Clean Energy* zkaf050 (2025) doi:10.1093/ce/zkaf050.

48. Pamungkas, M., Hidayatullah, W., Farista, F. & Masruroh, M. Investigation of Hydrogen Absorption on Iron-Nickel (FeNi) Alloy: A DFT Study of Thermodynamic Properties. (2024) doi:http://dx.doi.org/10.2139/ssrn.4951377.

49. Li, X., Ma, Y., Zhou, W. & Liu, Z. Hydrogen Atom and Molecule Adsorptions on FeCrAl (100) Surface: A First-Principle Study. *Front. Energy Res.* **9**, 1–11 (2021).

50. Ziemniak, S. E., Guilmette, P. A., Turcotte, R. A. & Tunison, H. M. Oxidative dissolution of nickel metal in hydrogenated hydrothermal solutions. *Corros. Sci.* **50**, 449–462 (2008).

51. Ziemniak, S. E. & Goyette, M. A. Nickel (II) Oxide Solubility and Phase Stability in High Temperature Aqueous Solutions. *J. Solution Chem.* **33**, 1135–1159 (2004).

52. Peng, Q., Hou, J., Sakaguchi, K., Takeda, Y. & Shoji, T. Effect of dissolved hydrogen on corrosion of Inconel Alloy 600 in high temperature hydrogenated water. *Electrochim. Acta* **56**, 8375–8386 (2011).

53. Peng, Q., Shoji, T., Hou, J., Sakaguchi, K. & Takeda, Y. Role of dissolved hydrogen in water in corrosion of alloy 600 in high temperature water. in *15th International Conference on Environmental Degradation* (eds. Busby, J. T., Ilevbare, G. & Andresen, P. L.) 1879–1892 (TMS (The Minerals, Metals & Materials Society), 2011, 2011).

54. Wallinder, D., Hörnlund, E. & Hultquist, G. Influence of Hydrogen in Iron and in Two Stainless Steels on Aqueous and Gaseous Corrosion. *J. Electrochem. Soc.* **149**, B393 (2002).

55. Hultquist, G., Tveten, B. & Hörnlund, E. Hydrogen in chromium: influence on the high-temperature oxidation kinetics in H2O, oxide-growth mechanisms, and scale adherence. *Oxid. Met.* **54**, 1–10 (2000).

56. Wallinder, D., Hultquist, G., Tveten, B. & Hörnlund, E. Hydrogen in chromium: Influence on corrosion potential and anodic dissolution in neutral NaCl solution. *Corros. Sci.* **43**, 1267–1281 (2001).

57. Tveten, B., Hultquist, G. & Norby, T. Hydrogen in chromium: Influence on the high-temperature oxidation kinetics in O2, oxide-growth mechanisms, and scale adherence. *Oxid. Met.* **51**, 221–233 (1999).